INCREMENTAL NONLINEAR DYNAMIC INVERSION CONTROLLER FOR A FLYING WING OPERATED IN AN AIRBORNE WIND ENERGY SYSTEM

D. F. Duda[1], H. Fuest[1], J. Müller[1], T. Islam[1] & D. Moormann[1]

[1]Institute of Flight System Dynamics (FSD), RWTH Aachen Unitversity, Germany

Abstract

This paper presents a controller for the motion of a flying wing embedded in an airborne wind energy system. In order to safely operate such a flying wing for dynamic flight maneuvers and with varying tether loads acting, a comprehensive control concept based on an incremental nonlinear dynamic inversion (INDI) with an incremental formulation of the control effectiveness is presented. A feature of this approach is its universal applicability, allowing unconventional maneuvers such as a multi-axial yaw-roll transition from hover to aerodynamic wing-borne flight. In addition to a detailed derivation of the effectiveness matrix, this paper presents the general architecture of the translational INDI controller, including a necessary quaternion-based attitude filter. Based on the presented controller implementation, the performance and limitations of this control approach are investigated. Results from nonlinear model-in-the-loop simulations and flight tests demonstrate the functionality of this control concept.

Keywords: motion controller, incremental nonlinear dynamic inversion (INDI), multi-axial yaw-roll transition, flying wing, quaternion based attitude filter

1. Introduction

The development of new technologies for using renewable energy sources, such as wind energy, has become increasingly important. Alongside established wind turbines, a new field of application for wind energy systems has been discovered through airborne wind energy (AWE). In these innovative energy systems, a flight system is operated in energy-rich winds while tethered to a winch on the ground to harvest electrical energy [1]. Figure 1 depicts one of these airborne wind energy systems (AWES) in the ground power generation (ground-gen) configuration. In such ground-gen AWES, the flight system applies a load to the tether during the so-called generation phase, which causes the tether to unwind from a drum on the winch and generates energy with a connected electrical generator. The airborne flight system exits the generation phase when the maximum tether length is reached. During the subsequent recovery phase, it flies back to its starting position, and the power generation phase begins again. An alternative airborne wind energy system configuration that is also intensively tested in this field is the flying power generation (fly-gen) AWES. Unlike the ground-gen AWES, the fly-gen system generates power directly through specialized onboard turbines installed along the wing as it flies in the wind field. As with ground-gen AWES, a tether binds the flying system to the ground; however, because a cable is integrated into the tether, it also transmits the generated electricity to the ground. A detailed description of this and other classifications of AWES can be found in [2]. A unique flight system configuration with the aerodynamic characteristics to optimize the power output for either configuration is the so-called flying wing. Here, the flight system is reduced to a single wing without horizontal stabilizers [3, 4, 5]. In addition, to allow vertical takeoff and landing directly at the ground station, independent of runways, this flying wing can be designed as tailsitter. As shown on the right side in Fig. 1, this configuration enables the flight system to take off and land sitting on its tail with its nose pointing upward [6, 7]. During takeoff and landing, the thrust of the

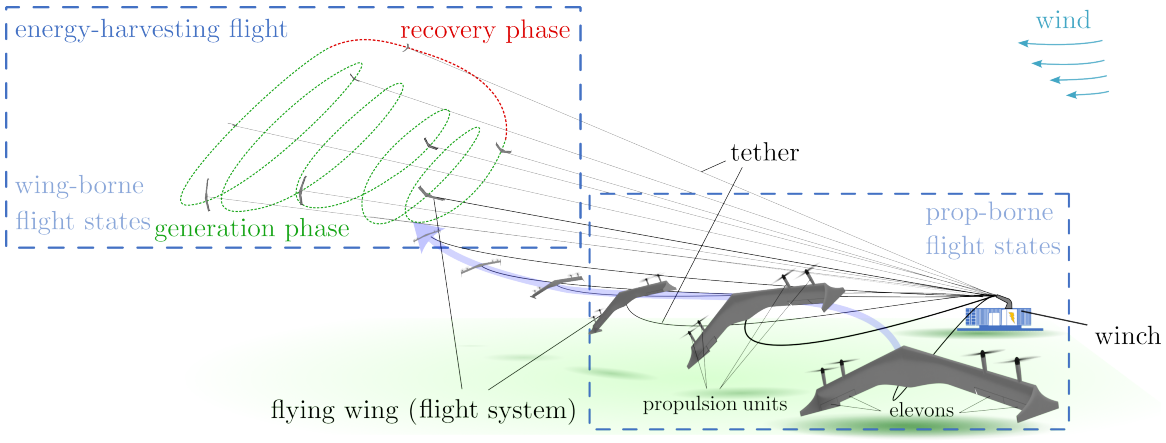

Figure 1 – General working principle of a flying wing AWES (shown for ground-gen configuration) and launching, including multi-axial yaw-roll transition from prop-borne flight states after vertical takeoff to wing-borne flight states with a tensioned tether.

propellers provides the complete lift. Within this phase, the flying wing adjusts the thrust direction to accelerate until the airflow around the wing generates lift. As airspeed and aerodynamic (wing) lift continue to increase, the flying wing can transition to an aerodynamic wing-borne flight and enter the energy-harvesting flight. For the transition from propeller-borne flight (hereafter abbreviated as prop-borne) to wing-borne flight, a multi-axial yaw-roll transition can be selected (see Fig. 1). In the context of airborne wind energy, an additional challenge for such an operation is that it must consider the tether acting on the so-called tether attachment point (TAP) of the flying wing as an additional constraint in force and geometry.

Within this contribution, we address the challenge of controlling the translational motion of such a flying wing during different flight phases. We focus on the launching, especially the dynamic multi-axial yaw-roll transition from prop-borne to wing-borne flight. In our recent work [8], we examine the challenges inherent in controlling the translational motion during a transition from a prop-borne flight to a wing-borne flight along a straight line without wind and tether interaction. A linear-quadratic controller based on specific operating states and model linearizations is used for the transition. Nevertheless, the required operational space is to be minimized when considering AWE wind farms. Consequently, a curved transition to and from energy harvesting flight becomes increasingly necessary. However, this expands the control problem, so the controller design architecture becomes very hard to handle with more state parameters while keeping a linear-quadratic control approach. In addition, the underlying model uncertainties and uncertainties related to changes in wind direction and intensity must be considered. Therefore, we have developed an approach to control the translational motion based on incremental nonlinear dynamic inversion (INDI). This approach requires less precise information about the system and can be designed comprehensively for the entire flight operation of the flying wing. In its basic form, this control approach is based solely on a formulation of control effectiveness.

When considering a translational motion INDI controller, the commanded attitude and thrust are considered virtual controls, while the translational acceleration is the controlled variable. In our previous work [9, 10], we have extensively dealt with controller architecture and control effectiveness for translational control of tiltwing flight systems. There, we consider only a longitudinal transition with control effectiveness formulated for a horizontal frame of reference. However, since the transition in our case is multi-axial, the control effectiveness formulation for a horizontal frame of reference cannot be applied here. In the following Sec. 2. an alternative approach using the body coordinate system as a reference frame with incremental attitude changes is presented. Based on this formulation of the control effectiveness, an introduction to the corresponding controller design is given. Since this sensor-based controller requires a filter of the acceleration signal, a corresponding filter of the control and, thus, of the attitude is necessary and introduced. The underlying guidance and rotational

controller are presented to complete the design of the entire flight controller. Within an analysis of the control concept for the translational motion in Sec. 3, a demonstrator and the corresponding model are introduced first. An analysis of the developed control effectiveness for a dynamic transition maneuver follows this. Based on this, results for a model-in-the-loop nonlinear analysis with the designed controller are presented and discussed. Finally, results of a first flight test with the proposed controller are presented before a conclusion, and the outlook of this work is given in Sec. 4.

2. Concept and architecture of translational control for a flying wing in AWE

Based on the work from [10, 11, 12, 13], the INDI control law can be formulated as given in Eq. (1). Here, $\vec{u}_c$ is the control variable sought, which can be composed of $\vec{u}_f$, the measured control, and an incremental control $\delta\vec{u}$. As shown, this incremental control can be formulated as the product of $\hat{\mathbf{B}}^{-1}$, the Moore–Penrose inverse of the control effectiveness matrix $\hat{\mathbf{B}}$, and the deviation between $\vec{\nu}$, the virtual command variable, and $\vec{x}_f$, the filtered state variable.

$$\vec{u}_c = \vec{u}_f + \delta\vec{u} = \vec{u}_f + \hat{\mathbf{B}}^{-1}\left(\vec{\nu} - \vec{\dot{x}}_f\right) \tag{1}$$

In order to formulate the effectiveness matrix $\hat{\mathbf{B}}$, it is first necessary to define the controls for the translational controller and a corresponding reference frame in which the translational motion is to be controlled. We propose considering the commanded throttle as the first entry for the translational control vector. It corresponds to an average thrust generated by the propulsion units of the flying wing. The remaining entries of this control vector can consider the flying wing's attitude. A change in attitude alters the direction of thrust and affects the airflow conditions. Consequently, the lift and drag forces acting on the flying wing change, resulting in a translational motion. One approach to include attitude as part of the control vector is to use Euler angles concerning a fixed reference frame, e.g., a fixed ground or horizontal coordinate system. However, the Euler angles vary significantly and in a nonlinear manner for any fixed reference frame for dynamic maneuvers such as the considered yaw-roll transition. Furthermore, singularity problems arise due to the wide range of attitude variations.

An alternative approach is to decouple the system into a reference frame fixed to the current body coordinate system and a control frame. In the control frame, the emerging forces are considered after the control has been applied, and thus, an incremental attitude change has occurred out of the current body coordinate system. At each time step, the current body frame and, thus, the reference frame are updated. The transformation between this reference frame and the control frame is described by incremental Euler rotation angles $[\delta\phi, \delta\theta, \delta\psi]$. Figure 2 illustrates this transformation relation between the reference frame $[\,]_b$ and the control frame $[\,]_{b^+}$. This allows the control vector to be defined as $\delta\vec{u} = [\delta f, \delta\phi, \delta\theta, \delta\psi]$. Therefore, the effect of each control in $\delta\vec{u}$ on the translational motion in the reference frame must be determined. In the following, the identification of this so-called control effectiveness matrix $\hat{\mathbf{B}}$ is presented.

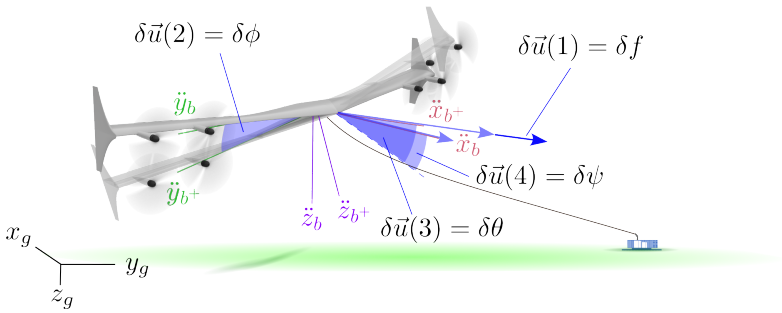

Figure 2 – Illustration of reference frame, control frame, and the corresponding incremental controls used to control the translational motion.

2.1 Derivation of control effectiveness matrix

The true effectiveness matrix $\mathbf{B}$ can be found by considering the product of the mass m of the flying wing and the difference of the external forces $\vec{F}$ acting on the center of mass of the flying wing before and after ($^+$) the application of the incremental control $\delta\vec{u}$. By excluding the control vector from this product, the control effectiveness matrix $\mathbf{B}$ can be found (see Eq. (2)).

$$\mathbf{B} \cdot \delta\vec{u} = \frac{1}{m}\left(\vec{F}_b^+ - \vec{F}_b\right) \tag{2}$$

In this paper, this control effectiveness matrix $\mathbf{B}$ is modeled for the controller design as $\hat{\mathbf{B}}$. Since the change in direction and magnitude of the weight force within the reference frame is not affected by the control $\delta\vec{u}$, the weight force can be disregarded in formulating the control effectiveness. Furthermore, if the tether is aligned approximately perpendicular to the wing, the tether force is also not directly affected by a change in the control $\delta\vec{u}$. Consequently, only the aerodynamic and thrust forces are considered in formulating the effectiveness matrix $\mathbf{B}$ for the INDI controller ((see Eq. 3)).

$$\hat{\mathbf{B}} \quad = \hat{\mathbf{B}}_\mathbf{T} + \hat{\mathbf{B}}_\mathbf{A} \tag{3}$$

A detailed derivation of the thrust and aerodynamic effectiveness matrix ($\hat{\mathbf{B}}_\mathbf{T}$, $\hat{\mathbf{B}}_\mathbf{A}$) is given in the following.

2.1.1 Thrust control effectiveness

To determine the effectiveness of the control vector regarding the thrust force $\vec{T}_b$, Eq. (2) can be specified and extended to the following form:

$$\begin{aligned} \hat{\mathbf{B}}_\mathbf{T} \cdot \delta\vec{u} &= \frac{1}{m}\left(\mathbf{M}_{\mathbf{bb}^+}\vec{T}_{b^+}^+ - \vec{T}_b\right) \\ &= \frac{1}{m}\left(\mathbf{M}_{\mathbf{bb}^+}\left(\vec{T}_b + \vec{\delta T}_b\right) - \vec{T}_b\right) \end{aligned} \tag{4}$$

Since the control $\delta\vec{u}$ respects an incremental change of attitude, it has to be considered that the thrust vector is rotated by a rotation matrix $\mathbf{M}_{\mathbf{bb}^+}$ (Euler angles $\delta\phi$, $\delta\theta$, $\delta\psi$) as follows:

$$\mathbf{M}_{\mathbf{bb}^+} = \begin{pmatrix} 1 & -\delta\psi & \delta\theta \\ \delta\psi & 1 & -\delta\phi \\ -\delta\theta & \delta\phi & 1 \end{pmatrix} \tag{5}$$

This rotation matrix considers the incremental rotation with the rotation order 'ZYX' (see Eq. (5)). Moreover, it is assumed that the incremental change in thrust $\delta\vec{T}_b$ is the product of the derivative $\partial\vec{T}_b/\partial f = [\frac{\partial T}{\partial f}, 0, 0]^T$ and δf. Considering that the mean thrust T is aligned with the four propeller axes, which are tilted by a small angle θ_p with respect to the wing ($\vec{T}_b = [\cos(\theta_p)T, 0, \sin(\theta_p)T]^T$), Eq. (4) can be reformulated as:

$$\hat{\mathbf{B}}_\mathbf{T} \cdot \delta\vec{u} = \frac{1}{m}\begin{pmatrix} \cos(\theta_p)\frac{\partial T}{\partial f}\delta f - \sin(\theta_p)T\delta\theta \\ \cos(\theta_p)T\delta\psi + \sin(\theta_p)T\delta\phi \\ -\sin(\theta_p)\frac{\partial T}{\partial f}\delta f - \cos(\theta_p)T\delta\theta \end{pmatrix} \tag{6}$$

Here, the incremental products (e.g., $\delta\phi \cdot \delta f \approx 0$) are neglected, which allows for determining a linear relationship between the control vector and the resulting acceleration from the change in thrust. Thus, the effectiveness matrix considering the thrust can be determined:

$$\hat{\mathbf{B}}_\mathbf{T} \quad = \begin{pmatrix} \frac{\cos(\theta_p)}{m}\frac{\partial T}{\partial f} & 0 & -\frac{\sin(\theta_p)}{m}T & 0 \\ 0 & \frac{\sin(\theta_p)}{m}T & 0 & \frac{\cos(\theta_p)}{m}T \\ -\frac{\sin(\theta_p)}{m}\frac{\partial T}{\partial f} & 0 & -\frac{\cos(\theta_p)}{m}T & 0 \end{pmatrix} \tag{7}$$

As shown, $\hat{\mathbf{B}}_\mathbf{T}$ depends only on the fixed geometric parameter θ_p as well as on the estimated thrust and the derivative of the thrust with respect to the throttle. These can be derived using a propulsion model.

2.1.2 Aerodynamic control effectiveness

Similar to identifying the thrust control effectiveness, the aerodynamic effectiveness can be determined as follows:

$$\hat{\mathbf{B}}_{\mathbf{A}} \cdot \delta\vec{u} \;=\; \frac{1}{m}\left(\mathbf{M_{ba^+}}\left(\vec{A}_a + \vec{\delta A}_a\right) - \mathbf{M_{ba}}\vec{A}_a\right) \tag{8}$$

Contrary to the thrust force, the aerodynamic force $\vec{A}_a$ cannot be described in a fixed orientation with respect to the body frame. Instead, it must be considered in an aerodynamic frame. As shown in Eq. (8), the transformation $\mathbf{M_{ba}}$ from the aerodynamic frame ($_a$) to the body frame ($_b$) is required. It is assumed that the airflow state can be estimated using a pitot tube and airflow vanes. This allows us to determine $\mathbf{M_{ba}}$ and to identify the state of the airflow in body coordinates as:

$$\vec{V}_a = \begin{pmatrix} u_a \\ v_a \\ w_a \end{pmatrix} \tag{9}$$

Moreover, the airflow in the $x-z$-plane can be considered as:

$$\vec{V}_{\bar{a}} = \begin{pmatrix} u_a \\ 0 \\ w_a \end{pmatrix} \tag{10}$$

For the sake of simplicity, the norm of $\vec{V}_a$ is abbreviated as V_a and the norm of $\vec{V}_{\bar{a}}$ as $V_{\bar{a}}$. If the current aerodynamic state of the airflow is known, the transformation $\mathbf{M_{ba}}$ can be formulated as:

$$\mathbf{M_{ba}} = \begin{pmatrix} \frac{u_a}{V_a} & -\frac{u_a v_a}{V_a V_{\bar{a}}} & -\frac{w_a}{V_{\bar{a}}} \\ \frac{v_a}{V_a} & \frac{V_{\bar{a}}}{V_a} & 0 \\ \frac{w}{V_a} & -\frac{v_a w_a}{V_a V_{\bar{a}}} & \frac{u_a}{V_{\bar{a}}} \end{pmatrix} \tag{11}$$

In addition to $\mathbf{M_{ba}}$, the corresponding transformation $\mathbf{M_{ba^+}}$, which takes into account the transformation of the aerodynamic frame after the control is applied ($_{a^+}$), is required in Eq. (8). This transformation can be computed as the product of the transformation $\mathbf{M_{ba}}$ and a transformation between the aerodynamic frames from before and after the control is applied ($\mathbf{M_{aa^+}}$). To identify this transformation between the aerodynamic frames, it can be assumed that the airflow does not change with respect to the reference body frame due to the control $\delta\vec{u}$. However, since the aerodynamic frame is defined by the orientation of the wing with respect to the airflow and the control $\delta\vec{u}$ considers a change in attitude, a transformation between the aerodynamic frames must be considered. This means that only the changing orientation of the wing has to be considered, which can be approximated by the incremental roll angle $\delta\phi$ of the control $\delta\vec{u}$. Thus, the transformation between the aerodynamic frames can be considered as:

$$\mathbf{M_{aa^+}} = \begin{pmatrix} 1 & 0 & 0 \\ 0 & 1 & -\delta\phi \\ 0 & \delta\phi & 1 \end{pmatrix} \tag{12}$$

This allows us to determine the transformation between the aerodynamic frames ($\mathbf{M_{ba^+}} = \mathbf{M_{ba}}\mathbf{M_{aa^+}}$). To extract the control vector from the left side of Eq. (8), the couplings of the incremental aerodynamic force $\vec{\delta A}_a$ and the control $\delta\vec{u}$ must be identified. Here, another assumption is made. Since the aerodynamic load depends on the change of the angle of attack, it can be extended to a formulation that considers the derivatives of the angle of attack and the control $\delta\vec{u}$:

$$\vec{\delta A}_a = \frac{\partial\vec{A}_a}{\partial\alpha^+}\frac{\partial\alpha^+}{\partial\vec{u}}\delta\vec{u} \tag{13}$$

Thus, a relation between the angle of attack and the control vector is required. The angle of attack considering the aerodynamic frame after the control is applied can be defined as:

$$\alpha^+ = \tan^{-1}\left(\frac{w_a^+}{u_a^+}\right) \tag{14}$$

Here, u^+ and w^+ can be determined using the measured airflow conditions in the body frame and the incremental coordinate transformation ($\mathbf{M_{b^+b}} = \mathbf{M_{bb^+}}^{-1}$). This allows the differentiation of Eq. (14) for the control vector. After simplifications, the derivative of the angle of attack can be formulated as:

$$\frac{\partial \alpha^+}{\partial \vec{u}} = \begin{pmatrix} 0 \\ -\frac{u_a v_a}{|\vec{V}_{\bar{a}}|_2^2} \\ 1 \\ \frac{u_a w_a}{|\vec{V}_{\bar{a}}|^2} \end{pmatrix} \tag{15}$$

The aerodynamic force derivatives required in Eq. (13) can be obtained as the product of the dynamic pressure, the wing area S, the drag derivative coefficients C_{D_α} and the lift derivative coefficients C_{L_α}:

$$\frac{\partial \vec{A}}{\partial \alpha^+} = \frac{\partial \vec{A}}{\partial \alpha} = \begin{pmatrix} D_\alpha \\ 0 \\ L_\alpha \end{pmatrix} = \frac{\rho |V_{\bar{a}}|_2^2}{2} S \begin{pmatrix} C_{D_\alpha} \\ 0 \\ C_{L_\alpha} \end{pmatrix} \tag{16}$$

Similar to our work in [9], the aerodynamic force $\vec{A}$ required in Eq. (8) can be estimated based on a force equilibrium of the translational motion, including the inertia loads from the measured accelerations, the measured tether force, and the estimated thrust computed by the propulsion model. With this, it is possible to determine all variables in Eq. (8), exclude the control $\delta\vec{u}$, and formulate the aerodynamic effectiveness $\hat{\mathbf{B}}_\mathbf{A}$ as:

$$\hat{\mathbf{B}}_\mathbf{A} = \begin{pmatrix} 0 & -\frac{\frac{A_y w_a}{V_a} - \frac{A_z u_a^2 v_a}{V_a V_{\bar{a}}^2} + \frac{D_\alpha u_a^2 v_a}{V_a V_{\bar{a}}^2} - \frac{L_\alpha u_a v_a w_a}{V_{\bar{a}}^3} + \frac{A_x v_a w_a}{V_a V_{\bar{a}}} - \frac{A_x u_a v_a w_a}{V_a^2 V_{\bar{a}}} + \frac{A_y u_a v_a^2 w_a}{V_a^2 V_{\bar{a}}^2}}{m} & \frac{D_\alpha u_a}{V_a} - \frac{L_\alpha w_a}{V_{\bar{a}}} \\ m & \\ 0 & -\frac{\frac{A_z u_a}{V_a} + \frac{A_x V_{\bar{a}} w_a}{V_a^2} - \frac{A_y v_a w_a}{V_a^2} + \frac{D_\alpha u_a v_a^2}{V_a u_a^2 + V_a w^2}}{m} & \frac{D_\alpha v}{V_a m} \\ 0 & \frac{\frac{A_y u_a}{V_a} - \frac{L_\alpha u_a^2 v_a}{V_{\bar{a}}^3} + \frac{A_x v_a w_a^2}{V_a^2 V_{\bar{a}}} - \frac{A_y v_a^2 w_a^2}{V_a^2 V_{\bar{a}}^2} + \frac{A_x u_a v_a}{V_a V_{\bar{a}}} + \frac{A_z u_a v_a w_a}{V_a V_{\bar{a}}^2} - \frac{D_\alpha u_a v_a w_a}{V_a V_{\bar{a}}^2}}{m} & \frac{L_\alpha u_a}{V_{\bar{a}}} + \frac{D_\alpha w_a}{V_a} \\ & m & \end{pmatrix} \begin{matrix} -\frac{v_a w_a (V_{\bar{a}}\ D_\alpha u_a - V_a L_\alpha w_a)}{V_a V_{\bar{a}}^3 m} \\ -\frac{D_\alpha v_a^2 w_a}{V_a V_{\bar{a}}^2 m} \\ -\frac{v_a w_a (V_a L_\alpha u_a + V_{\bar{a}} D_\alpha w_a)}{V_a V_{\bar{a}}^3 m} \end{matrix} \tag{17}$$

Again, products of small increments (e.g., $\delta\phi \cdot \delta\psi \approx 0$) are neglected to obtain a linear relationship between the control vector and the change in aerodynamic force. This allows us to complete the effectiveness matrix $\hat{\mathbf{B}}$ using Eq. (3).

2.2 Control allocation problem formulation

In the proposed form of the INDI translational controller with a four-dimensional control vector $\delta\vec{u} \in \mathbb{R}^4$ and three translational accelerations fixed to the body frame as controlled variables $\vec{x} \in \mathbb{R}^3$, the controlled system is overdetermined. Thus, extending the control problem of Eq is possible. (1) by an allocation. This allocation also allows for suitable desired incremental controls $\delta\vec{u}_d$ by using weighting terms. Furthermore, it is possible to assign weighting terms to consider rates of change of the control $\delta\vec{u}$. Within the allocation, this allows to formulate a cost function $\mathbf{I}$ that is minimized for the sought control $\delta\vec{u}$:

$$\begin{aligned} \mathbf{I} = \quad & ||\mathbf{W_y}\left[\left(\vec{\nu} - \vec{\dot{x}}_f\right) - \hat{\mathbf{B}}\delta\vec{u}\right]||_2^2 + ||\mathbf{W_r}\delta\vec{u}||_2^2 \\ & + ||\mathbf{W_d}\left(\delta\vec{u} - \delta\vec{u}_d\right)||_2^2 \end{aligned} \tag{18}$$

Here, $\mathbf{W_y}$, $\mathbf{W_r}$, $\mathbf{W_d}$ are the weighting matrices of the control deviation, rate, and desired control. The desired control vector $\delta\vec{u}_d$ consists of the four incremental desired control states $[\delta f_d, \delta\phi_d, \delta\theta_d, \delta\psi_d]$. For example, during the yaw-roll transition from a prop-borne to a wing-borne flight state, the actual roll motion must be commanded using an incremental desired command $\delta\phi_d \neq 0$. Otherwise, the flying wing could remain in a prop-borne flight state with a high sliding angle. Within the controller design, Eq. (18) is reformulated as a quadratic optimization problem and solved according to [14] using the active set method for each time step.

2.3 Control architecture

Following Binz [10] and Smeur [15], the general architecture of the translational INDI control approach without considering an allocation is shown in Fig. 3. For the translational INDI controller, $\vec{x}$ considers the body velocity vector, and $\vec{\dot{x}}$ is the corresponding acceleration. As shown in Fig. 3 and given in Eq. (1), the measured acceleration is filtered by $H(s)$ before the deviation to the commanded acceleration $\vec{\dot{x}}_c$ is determined. Using the inverse of the control effectiveness $\hat{\mathbf{B}}$, the incremental control $\delta\vec{u}$ can be determined. To avoid manipulation of the overall transfer behavior by this filter, it must also be considered in the inner accumulation loop of the control. Within this inner loop, $G(s)_{actuator}$ considers the actuator's dynamics. In this linear formulation, the plant is represented by the system matrix $\mathbf{A}$ and the input matrix $\mathbf{B}$. For an ideal transfer behavior of the INDI controller, i.e., the effectiveness of the plant and that modeled for the control are equal ($\mathbf{B} = \hat{\mathbf{B}}$)), the transfer behavior from the commanded acceleration $\vec{\dot{x}}_c$ to the acceleration $\vec{\dot{x}}$ is equal to the transfer behavior of the actuator $G(s)_{actuator}$ (see [15]).

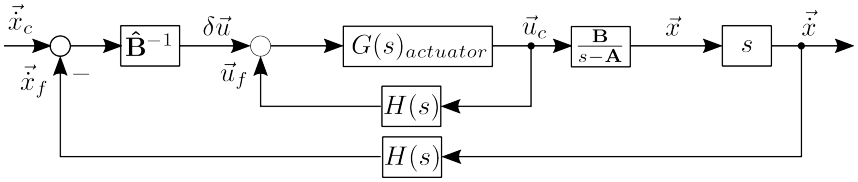

Figure 3 – General architecture of the translational INDI control loop.

The entire translational INDI control architecture is implemented in the overall flight controller illustrated in Fig. 4. Similar to the control architecture in [9], this flight controller has a cascaded structure with a guidance controller on the highest level. This guidance controller determines the acceleration command required to keep the flying wing on a given trajectory, with the option to also control the

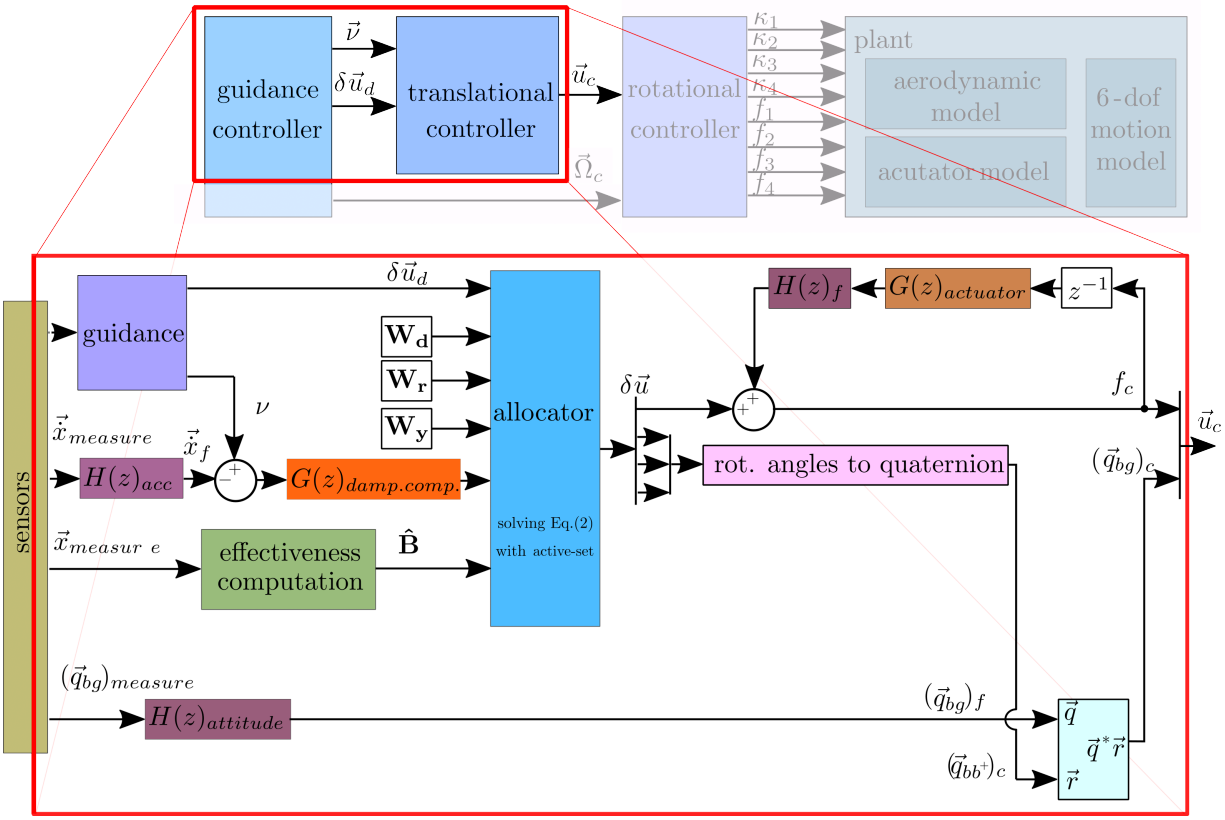

Figure 4 – Cascaded control architecture similar to [9] and structure of the translational INDI controller.

tether force in a wing-borne tethered flight. In addition, it outputs the desired $\delta\vec{u}_d$, depending on the current operation state. To ensure a curve coordinated flight, the guidance also outputs the required angular rate. The rotational controller is at the lowest level of the cascaded controller. As shown in Fig. 4, for the given flying wing, this rotational controller outputs four elevons (κ_{1-4}) and four throttle commands for the four propulsion units ($f1-4$). The prescribed mean thrust and attitude commands that compose the control vector $\vec{u}_c$ of the translational INDI controller serve as inputs to the rotational controller. In addition, the angular rate commanded by the guidance is considered an input. In this work, the rotational controller comprises a rotational INDI controller and an LQR controller. Based on the commanded and measured attitude and the commanded and measured angular rate, the LQR controller determines a rotational acceleration command. Within the rotational INDI controller, this command and the measured rotational acceleration are used to determine the elevons and throttle commands using their control effectiveness. This rotational controller and validating flight tests are detailed in [16].

The translational controller is on the intermediate level between the guidance and the rotational controller. Its structure is detailed in Fig. 4. In contrast to the illustration in Fig. 3, the translational INDI controller is presented in a time-discrete formulation. As shown, the filtered acceleration from the IMU-Sensor is subtracted from the acceleration command from the guidance. In contrast to the general architecture shown in Fig. 3, an additional damping compensation is considered here. According to [10], such damping compensation can be formulated as:

$$G(z)_{damp.comp.} = \frac{(1 - Z_w \Delta T)z - 1}{z - 1} \tag{19}$$

Due to the large wing area, the damping Z_w in z_b-direction is the most dominant damping and is therefore compensated for the current flight state. It considers the airflow conditions and the previously (z^{-1}) commanded mean throttle. The current flight state is also used to determine the overall effectiveness matrix $\hat{\mathbf{B}}$ using Eq. (3). The compensated command deviation, the effectiveness matrix $\hat{\mathbf{B}}$, and the incremental desired control command $\delta\vec{u}_d$ (output from the guidance) are inputs for the allocator. In addition, weighing parameters $\mathbf{W_d}$, $\mathbf{W_r}$ and $\mathbf{W_y}$ are considered. Within the allocator, the optimization problem Eq. (18) is solved allowing to obtain the incremental control $\delta\vec{u}$. Following the illustration of the general INDI control structure in Fig. 3, this incremental control is added on a measured or estimated previous control vector $\vec{u}_{c,k-1}$. As the actual throttle control is difficult to measure, an inner accumulation loop with the modeled actuator dynamics $G(z)_{acutator}$ is considered. Regarding the attitude command, a gyro sensor can measure the current flight attitude. Both the estimated throttle and measured attitude are also filtered. Following Binz [10], the filter implemented here is considered as PT2 transmission element with damping D and cut-off frequency ω_f.

$$H(s) = \frac{\omega_f^2}{s^2 + 2D\omega_f + \omega_f^2} \tag{20}$$

This filter is translated into time-discrete formulation using, for example, the Tustin approximation $s = \frac{2}{\Delta t}\frac{z-1}{z+1}$. The time-discrete formulation of this filter $H(z)$ is used for the acceleration and the throttle signal. However, the filtering of the attitude cannot be accomplished this way. The difficulty here is to achieve a suitable interpolation between different attitudes. One approach to achieve such an interpolation is the spherical linear interpolation introduced by Shoemake [17]:

$$\vec{q}_{slerp,01} = \frac{\sin[(1-\alpha_{slerp})\Omega_{slerp}]}{\sin\Omega_{slerp}}\vec{q}_0 + \frac{\sin[\alpha_{slerp}\Omega_{slerp}]}{\sin\Omega_{slerp}}\vec{q}_1 \tag{21}$$

Here, $\vec{q}_{slerp,01}$ considers the quaternion of the spherical linear interpolation between the normalized quaternions $\vec{q}_0$ and $\vec{q}_1$ with the interpolation factor $0 \leq \alpha_{slerp} \leq 1$. Ω_{slerp} denotes the angle subtended by the arc, so that $\cos(\Omega_{slerp}) = \vec{q}_0 \cdot \vec{q}_1$ is the dot product of the origin attitude q_0 and the final attitude $\vec{q}_1$. If the subtended angle Ω_{slerp} is close to zero, a linear interpolation can be used:

$$\vec{q}_{lerp,01} = (1-\alpha_{slerp})\vec{q}_0 + \alpha_{slerp}\vec{q}_1 \tag{22}$$

This slerp algorithm can also be formulated where $\vec{q}_0$ is the previously computed spherical interpolation and $\vec{q}_1$ is the current input at time step $_k$. If the interpolation factor α_{slerp} is to characterize the dynamic interpolation between these two attitudes as α_{filter}, then Eq. (21) and Eq. (22) can be formulated as:

$$\begin{aligned} \vec{q}_{k,y} = &\quad \frac{\sin[(1-\alpha_{filter})\Omega_{slerp}]}{\sin\Omega_{slerp}}\,\vec{q}_{k-1,y} + \frac{\sin[\alpha_{filter}\Omega_{slerp}]}{\sin\Omega_{slerp}}\,\vec{q}_{k,u} \quad |\Omega_{slerp} > 1^\circ \\ \vec{q}_{k,y} = &\quad (1-\alpha_{filter})\,\vec{q}_{k-1,y} + \alpha_{filter}\,\vec{q}_{k,u} \quad |\Omega_{slerp} \leq 1^\circ \end{aligned} \tag{23}$$

Here, $\vec{q}_{k,y}$ and $\vec{q}_{k-1,y}$ consider the current and previous output, whereas $\vec{q}_{k,u}$ considers the current input. This formulation is similar to the time-discrete difference equation of a PT1 element:

$$y_k = y_{k-1} + (u_k - y_{k-1})\,\underbrace{\frac{\Delta t}{T_{filter}+\Delta t}}_{\alpha_{filter}} \tag{24}$$

where y_k considers a linear interpolation between the input value u_k and the previously calculated output state y_{k-1} with the interpolation factor α_{filter}. The interpolation factor α_{filter} comprises the time constant T_{filter} and the sampling time Δt. This allows the time-discrete slerp formulation from Eq. (23) to be assigned the transfer characteristic of a PT1 element. The cut-off frequency is considered within the interpolation factor as $\omega_{f,slerp} = \omega_{PT1} = 1/T_{PT1}$. Since two equal PT1 elements connected in series form a PT2 element, a serial combination of two of these PT1 slerp filters corresponds to a filter with a PT2 transfer characteristic:

$$G_{PT2} = G_{PT1}\cdot G_{PT1} = \frac{K_{PT1}}{1+T_{PT1}\,s}\cdot\frac{K_{PT1}}{1+T_{PT1}\,s} = \frac{K_{PT1}\cdot\left(\frac{1}{T_{PT2}}\right)^2}{s^2+2\frac{1}{T_{PT1}}+\left(\frac{1}{T_{PT2}}\right)^2} = \frac{K_{PT2}\cdot\left(\frac{1}{T_{PT2}}\right)^2}{s^2+2D\frac{1}{T_{PT2}}+\left(\frac{1}{T_{PT2}}\right)^2} \tag{25}$$

However, as Eq. (25) shows, the damping D of such slerp-based PT2 filter is restricted to $D = 1$. The developed attitude slerp-based filter is implemented in Matlab Simulink. In the following, the functionality of the slerp-based attitude filter is presented for a representative test case shown in Fig. 5a. It is assumed that the flying wing is in a hovering flight state with the nose pointing upward. As shown in Fig. 5b, the initial pitch angle is $\theta = 85°$, while the roll and yaw angles are zero ($\phi = \psi = 0°$). Assuming a pitch step of $+\Delta\theta = 10°$ and considering the rotation order 'ZYX', the roll and yaw angles

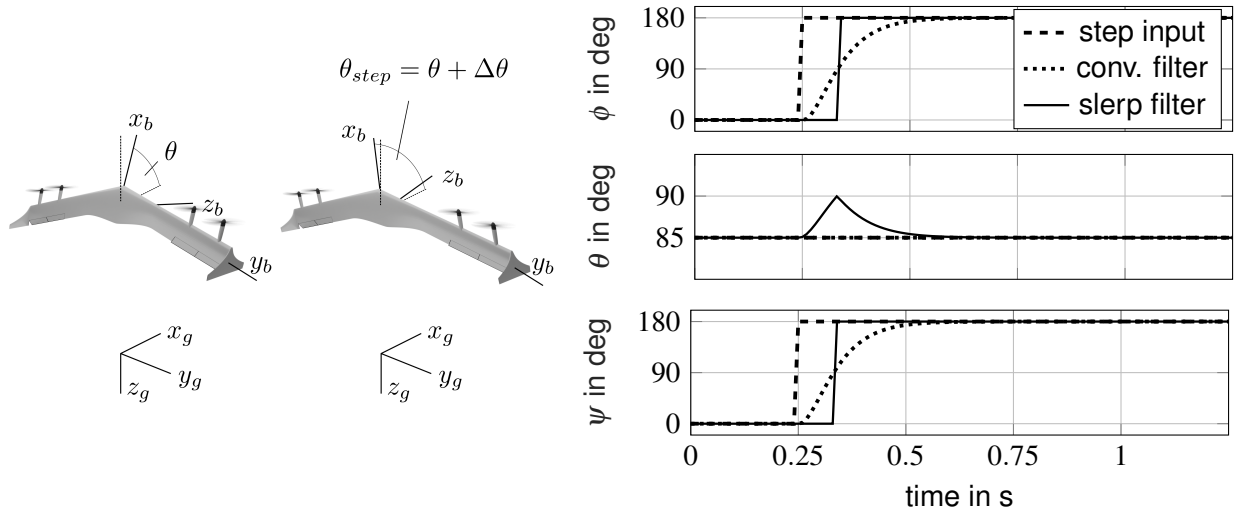

(a) Illustration of attitude before and after $\Delta\theta$

(b) Euler angles for pitch step in hover flight.

Figure 5 – Pitch attitude change in hover flight. The index $_f$ considers the filtered euler signals using a regular PT2 filter, whereas the index $_{q,f}$ considers the filtered euler angles using the slerp-based filter ($\omega_f = 40$ rad/s, $D = 1$).

jump to $\phi = \psi = 180°$, while the pitch angle remains at $\theta = 85°$. The resulting attitude is shown in the Fig. 5a. Once the attitude angles (ϕ, θ, ψ) are filtered independently, the flying wing performs a coupled roll and yaw motion instead of a simple pitch motion. Due to the attitude step, ϕ and ψ increase from 0° to 180°. The implemented slerp-based attitude filter allows filtering the attitude independent of the Euler angles. As shown in Fig. 5b, the filtered attitude considers a pitch motion up to 90°. From there, the roll and yaw angles jump to 180°, and the pitch angle decreases to 85°, resulting in the attitude shown in Fig. 5b. Thus, the slerp filter results in a simple pitch motion. This shows that the developed slerp filter is, in principle, suitable for attitude filtering. To verify that the transfer behavior is equivalent to that of a PT2, the response behavior for a pitch angle step of 1° in θ is considered. In contrast, the initial Euler angles are all set to zero. Below, Fig. 6 shows the step responses for both a PT1 and a PT2 as conventional and slerp-based elements. As can be seen, the slerp-based and conventional PT1 and PT2 show the same response behavior. For both, the damping is set to 1, and in the given test case, the cut-off frequency is set to $\omega_f = 40$ rad/s. This proves that the developed slerp filter can be used for the translational INDI controller.

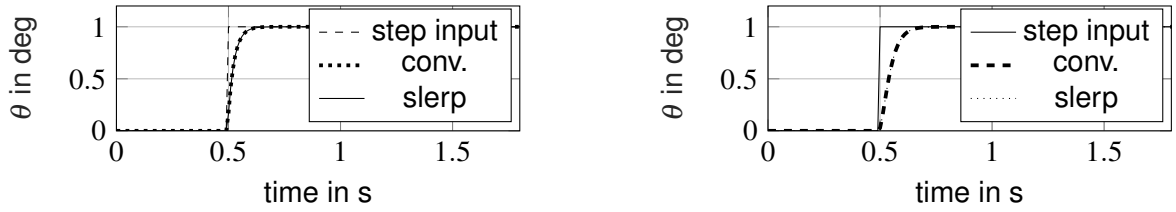

(a) PT1 step response ($\omega_f = 40$ rad/s)

(b) PT2 step response ($D = 1, \omega_f = 40$ rad/s)

Figure 6 – Step response of conventional and slerp based PT1 and PT2

3. Analysis of translational controller

A flying wing demonstrator and the corresponding model are presented below. Based on this, an implementation of the presented control effectiveness considered in the controller design is compared with one obtained from model linearization. Then, the control concept is analyzed using a nonlinear model-in-the-loop simulation. In addition to analyzing the simulation results, the results of a flight test are presented and analyzed.

3.1 Demonstrator

The flying wing under consideration is shown in Fig. 7. Configured as tailsitter it can take off and land standing on its wiglets. This demonstrator has a mass of 3.5 kg, spans about 2 m, and is equipped with four elevons and propulsion units - two on each side of the wing. Each propulsion unit can generate a maximum thrust of about 18 N. The elevons are designed with a relatively large surface and can deflect almost 30° in each direction. In contrast to other tailsitters studied by academia [18, 19, 20], the aspect ratio of this flying wing demonstrator is up to two times higher in order to reduce induced

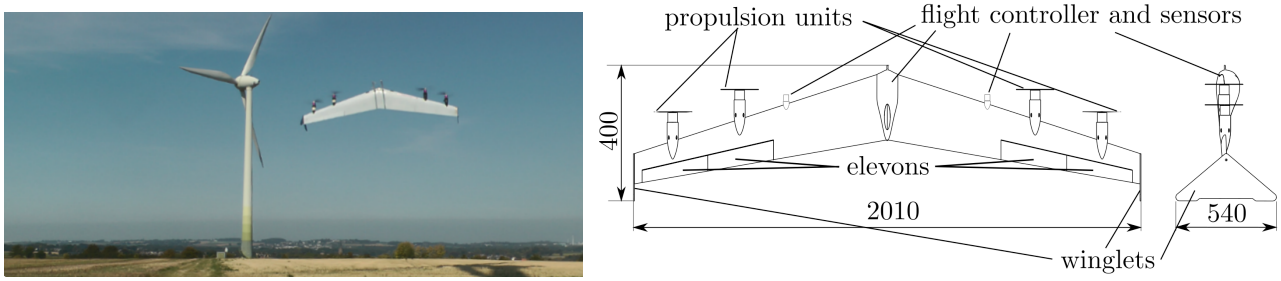

(a) Demonstrator in flight test.

(b) Sketch with descriptions and dimensions.

Figure 7 – Demonstrator.

drag, enhance the aerodynamic performance, and improve the potential performance in an AWE context. Overall, this small-scale demonstrator is intended to be comparable to future demonstrators designed primarily for energy-harvesting flight and is thus driven by aerodynamic efficiency. However, this comes with control limitations as shown in [16], where an upscale of this demonstrator is presented.

The flight controller is a specially developed circuit board with a clock rate of 200 Hz. Most of the sensors used on the flying wing measure the current state of motion. The angular rate and acceleration sensors are integrated into an Inven Sense MPU-6000 micromechanical system, also known as an inertial measurement unit (IMU). In addition, a satellite navigation receiver of the type Novatel OEM-618D is used and operated differentially to a base station. The receiver uses the Real-Time-Kinematic (RTK) method, which allows positions to be measured with an accuracy of a few centimeters. It is also possible to estimate the azimuth using two antennas, one on each side of the wing and positioned close to the leading edge. In addition, an onboard magnetometer can be used to obtain the azimuth. Aggregating the measured variables into an estimate of the current inertial motion state follows the description in [21] in the sense of a loosely coupled system. See also[22] for a detailed description.

For flight control, it is essential to determine the adequate aerodynamic airflow conditions during flight. However, since the flying wing is expected to operate at high sideslip angles during the multi-axial yaw-roll transition, more than a conventional fixed pitot system aligned with the flying wing's longitudinal axis is insufficient. These pitot tubes only allow an angular airflow offset of less than 10°. However, sideslip angles close to 90° are expected during the yaw-roll transition. Therefore, our flying wing is equipped with a wind vane that measures the airflow's direction within the wing's plane (see Fig 8). A servo that controls the alignment of a pitot tube can then be actively guided to the measured wind vane position and thus to the expected main direction of airflow (assuming an operation with a low angle of attack). Since the wind vane and pitot tube measurements require an airflow of at least 5-6 m/s to provide meaningful results, a wind measurement at the winch is also included in estimating the aerodynamic airflow condition.

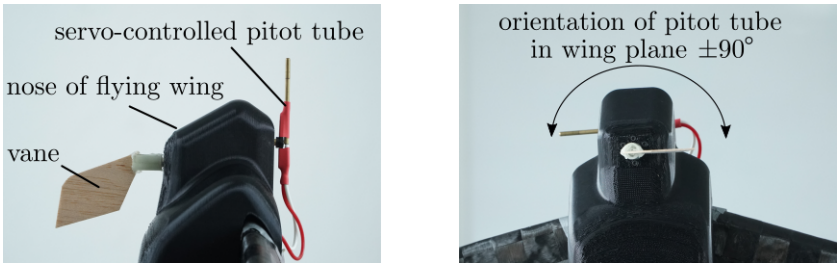

Figure 8 – Estimation of aerodynamic airflow using servo-controlled pitot tube and a vane.

The tether used has a diameter of 2 mm, a length of 75 m, and is of Dyneema type, known for its high strength and low weight. In the context of this paper, the focus is on the dynamic transition maneuver during launching. It is assumed that during this maneuver, the flying wing operates without an actively controlled winch so that the winch can be considered as an anchor point of the tether on the ground, and the tether length is considered fixed.

3.2 Model of demonstrator

According to the assumptions made for the controller design, the flying wing is modeled as a rigid body with mass m and six degrees of freedom. The translational motion is described by Eq. (26).

$$\begin{bmatrix} \dot{u} \\ \dot{v} \\ \dot{w} \end{bmatrix}_b = \mathbf{M}_{ba} \begin{bmatrix} \frac{D}{m} \\ \frac{D_e}{m} \\ \frac{L}{m} \end{bmatrix}_a + \begin{bmatrix} \frac{cos(\theta_p)T}{m} \\ 0 \\ \frac{sin(\theta_p)T}{m} \end{bmatrix}_b + \mathbf{M}_{bg} \begin{bmatrix} 0 \\ 0 \\ g \end{bmatrix}_g + \mathbf{M}_{bt} \begin{bmatrix} 0 \\ 0 \\ \frac{F_t}{m} \end{bmatrix}_t + \begin{bmatrix} p \\ q \\ r \end{bmatrix}_b \times \begin{bmatrix} u \\ v \\ w \end{bmatrix}_b \tag{26}$$

Here, $[u\ v\ w]^T$ denotes the translational velocity and $[p\ q\ r]^T$ the rotational velocity. In addition to the inertia loads, the thrust is represented by T and tilted by a small offset angle θ_p with respect to the wing-plane. As in the formulation of the aerodynamic effectiveness (see Sec. 2.1.2), the aerodynamic loads are represented in the aerodynamic frame $[\,]_a$ by lift L and drag D and D_e. They are transformed to the body frame using the coordinate transformation $\mathbf{M}_{[ba]}$. Similarly, gravity and tether force are transformed to the body-fixed frame using $\mathbf{M}_{[bg]}$ and $\mathbf{M}_{[bt]}$. In addition to the translational motion, the angular motion can be described by Eq. (27), where $[\dot{p}\ \dot{q}\ \dot{r}]^T$ are the body-fixed rotational accelerations, I is the inertia tensor, and $[M_x\ M_y\ M_z]^T$ includes all external moments. The external moments are those generated by thrust, by the deflection of the elevons, and by the airflow on the wing. Since the tether force is assumed to act on the center of mass, the tether generates no additional moment.

$$\begin{bmatrix} \dot{p} \\ \dot{q} \\ \dot{r} \end{bmatrix}_b = I^{-1} \left[\begin{bmatrix} M_x \\ M_y \\ M_z \end{bmatrix}_b - \begin{bmatrix} p \\ q \\ r \end{bmatrix}_b \times \left(I \cdot \begin{bmatrix} p \\ q \\ r \end{bmatrix}_b \right) \right] \tag{27}$$

The aerodynamic model of the flying wing is based on the semi-analytical element approach, according to Hartmann [22]. In this approach, the wing is decomposed into a discrete number of elements, considering each element's airflow. The aerodynamic forces and moments are computed at each element based on the given airfoil and airflow conditions. For those elements that also consider a propulsion unit (propulsion elements $i = 1...4$), the generated thrust ($T_i = T_i(f,u)$), depending on the current throttle and airflow, is determined. The resulting aerodynamic, thrust, and gravitational forces and moments are summed for all wing elements. In order to adequately model the dynamics of the tether and to keep it suitable for online model-in-the-loop simulations, the model from [23] is used. In this work, it is assumed that the length of the tether remains constant throughout the considered operational phases, allowing it to neglect any winch dynamics.

3.3 Analysis of control effectiveness matrix

To prove that the effectiveness matrix $\hat{\mathbf{B}}$ developed for the INDI controller is implemented with sufficient accuracy, it is compared with the effectiveness matrix obtained from a model linearization $\mathbf{B}$ (compare Fig. 9b). The linearization performed here is similar to Hartmann [22]. The Jacobian matrix is determined by varying the throttle and attitude for a given operating point and identifying the resulting motion in the body frame of the operating point. Again, regarding the change in attitude, the rotation order is kept to 'ZYX'. This allows us to determine the change in the acceleration in the body frame due to these controls (incremental change in throttle (δf) and attitude ($\delta\phi$, $\delta\theta$,$\delta\psi$)). Here, 20 operating points are considered along a straight yaw-roll transition (visualization in Fig. 9a) from propeller-borne hover flight with an airflow of 0 m/s to a wing-borne flight with an airflow of 13.5 m/s. These operating points are derived in our work in [8]. The derivatives respecting the same body axis are shown in the same subplot for illustration reasons. This allows us to better compare the effectiveness of the different controls on the considered motion.

As the thrust has a considerable impact on the x_b-motion, the corresponding derivative $\hat{\mathbf{B}}_{x,\delta f}$ is the dominant derivative throughout the entire transition. However, an increase in the effectiveness of the other controls can be identified for airspeed greater than 6 m/s. Regarding the y_b-motion, the incremental yaw control $\hat{\mathbf{B}}_{y,\delta\psi}$ is the most dominant control for the first 6 m/s. For airflows above 6 m/s, the roll control $\hat{\mathbf{B}}_{y,\delta\phi}$ becomes more dominant. Regarding the z_b-motion, the roll $\hat{\mathbf{B}}_{z,\delta\phi}$ and pitch control $\hat{\mathbf{B}}_{z,\delta\theta}$ dominate throughout a large part of the transition. However, for increasing airspeed above 12 m/s, the pitch motion dominates especially. When considering the dominant controls for each axis, the relative deviation between the computed derivatives from the plant and the one from the INDI controller is below 20% for most parts of the transition. According to a linear robustness analysis of the INDI control concept in [10], such a deviation is within the stability limits. This proves that the presented method for calculating the effectiveness is suitable. A better match between the control effectiveness from the linearization $\mathbf{B}$ and the one from the INDI control $\hat{\mathbf{B}}$ could be achieved by extending the aerodynamic effectiveness calculation. So far, it has not been considered that the

wake flow significantly changes the local airflow conditions. For example, at low airspeed in a prop-borne hovering flight, the wing elements with propulsion units experience a relevant airflow due to the wake flow of the propeller so that local lift forces are generated locally. A differentiated consideration of the wing in areas where a propeller wake flow occurs and in areas where only the free airflow is considered could improve the formulation of the control effectiveness but may lead to significant challenges in the linearization and extraction of the control effectiveness matrix $\hat{\mathbf{B}}$.

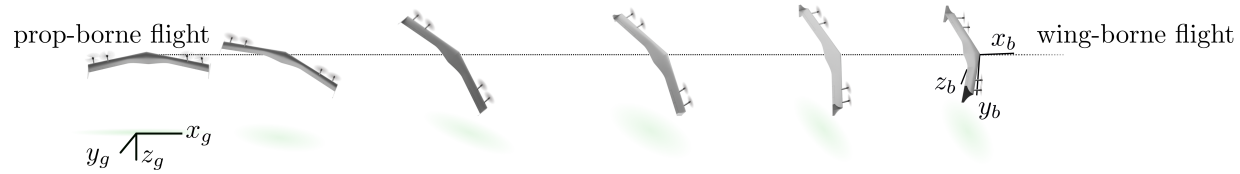

(a) Untethered straight yaw-roll transition.

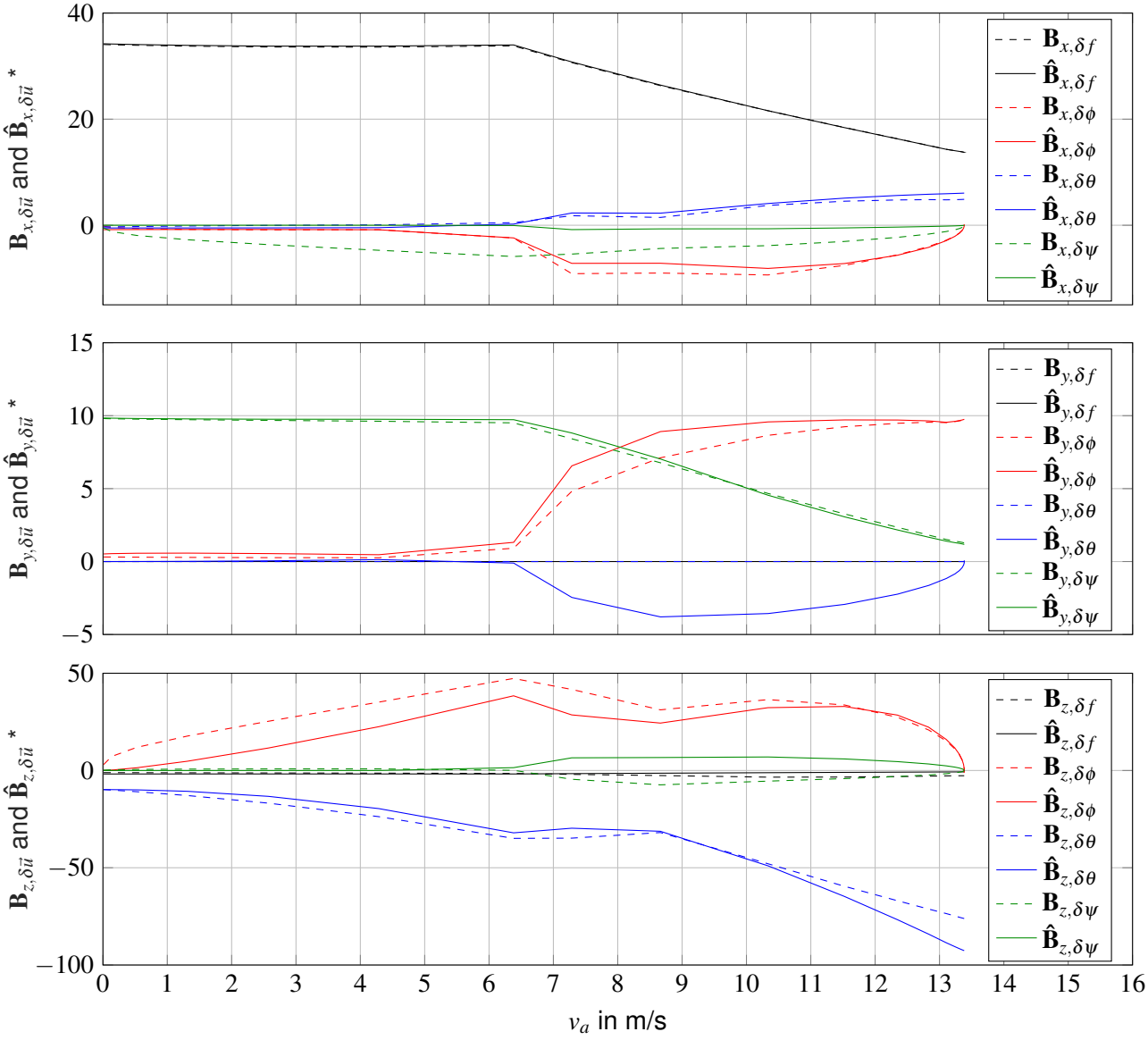

* in m/(s^{2}rad) or m/(s^2)

(b) Corresponding control effectiveness $\mathbf{B}$ from a linearization of the model and that of the controller $\hat{\mathbf{B}}$.

Figure 9 – Analysis of control effectiveness for a representative dynamic maneuver.

3.4 Analysis of INDI controller via model-in-the-loop simulations

The complete translational controller, the presented underlying guidance, and the rotational controller have been implemented and integrated in a model-in-the-loop environment in MATLAB-Simulink. The complete set of equations of motion given in Eq. (26) and Eq. (27) is solved for each simulation step. In the following, the control performance is analyzed for two scenarios. In the first one, the focus is placed on the dynamic transition maneuver from a propeller-borne hover flight to a wing-borne flight along a straight line, as shown in Fig. 9a, whereas the second one considers the tethered transition from prop- to wing-borne flight on a curved path in a wind field with a subsequent tether force control phase (see Fig. 11a).

For the first scenario, the results of the model-in-the-loop simulation are given in Fig. 10. The first three plots in Fig.10 show the indicated airspeed (IAS), the Euler angles $\vec{\Phi}$ in rotation order 'ZXY', and the transition ratio tr meaning the ratio of lift and gravitational load. These three plots help to identify the flight state throughout the simulation. During the first 25 s, the flying wing accelerates to an airspeed of 16 m/s while the pitch angle decreases from about 90° to 6°. It is during the acceleration phase that the actual transition begins. Here, the state of the transition can be estimated by the transition ratio tr, which goes from values close to 0 during the prop-borne hovering phase at lower airspeed to values close to 1, indicating an aerodynamic wing-borne flight at airspeed above 15 m/s. With a focus on the performance of the translational INDI controller, the estimated translational accelerations ($_{est}$) and the corresponding measured accelerations ($_f$) are also observed (see the last three plots in Fig.10). Here, the estimated acceleration takes into account a filtering of the commanded acceleration using the actuator dynamics $G(z)_{actuator}$ and the filter $H(z)$ according to Eq. (28), while the measured acceleration considers a filtering of the acceleration measured with the IMU sensor and filtered with $H(z)$ according to Eq. (29) (see Binz [10]). In doing so, the actuator dynamics correspond to the considered transmission behavior of the closed-loop attitude controller, e.g., the transmission behavior of the pitch motion ($G(z)_{actuator} = \frac{\theta(z)}{\theta(z)_{cmd}}$).

$$\vec{\dot{x}}_{est} = G(z)_{actuator} \cdot H(z) \cdot \vec{\dot{x}}_c \tag{28}$$

$$\vec{\dot{x}}_f = H(z) \cdot \vec{\dot{x}}_{measured} \tag{29}$$

As shown in Fig. 10, during the actual acceleration phase (0 - 15 s), the acceleration in the y_b-direction is controlled with an error between the estimated and measured acceleration of less than 20%. The error is less than 5 % in the other body axes. Within this analysis, the squared deviation error between estimated ($_{exp}$) and measured ($_f$) acceleration is integrated over a time frame as shown in Eq. (30) for all three body axis (index $i \in [1,2,3]$) of the acceleration vector.

$$J(i) = \int_{t_{start}}^{t_{end}} |\vec{\dot{x}}_{est}(i) - \vec{\dot{x}}_f(i)|^2 dt \tag{30}$$

For the first 15 s, this measure of control quality is 0.02 m^2/s^3 and 0.24 m^2/s^3 for the accelerations in x_b- and z_b-direction and 0.48 m^2/s^3 for the one in y_b-direction. In the following roll phase (15 s - 34 s), associated with fast attitude changes and a rapid increase of the transition ratio to 1, the errors increase in all three axes. However, in contrast to the previous acceleration phase, the errors in x_b- and z_b-direction are higher than the ones in y_b-direction. The integrated error in y_b-direction is only 0.73 m^2/s^3, while the integrated error in x_b-direction is 1.12 m^2/s^3 and the one in z_b-direction is 4.52 m^2/s^3. Since damping compensation is considered in the controller design, this increase in error can be explained mainly by the error in the formulation of the effectiveness matrix presented in the previous section. It is noticeable that, especially in z_b-direction, the error is higher than in x_b-direction. Since the aerodynamic force is dominant in z_b-direction and the thrust is dominant in x_b-direction, this indicates that the estimation of the aerodynamic effectiveness is less accurate than that of the thrust. On the other hand, since the implemented damping compensation only considers the dominant damping in z_b-direction and is determined based on discrete interpolation points, an error resulting from the damping cannot be eliminated. Nevertheless, the overall estimated and measured accelerations strongly correlate. This indicates the functionality of the translational INDI controller.

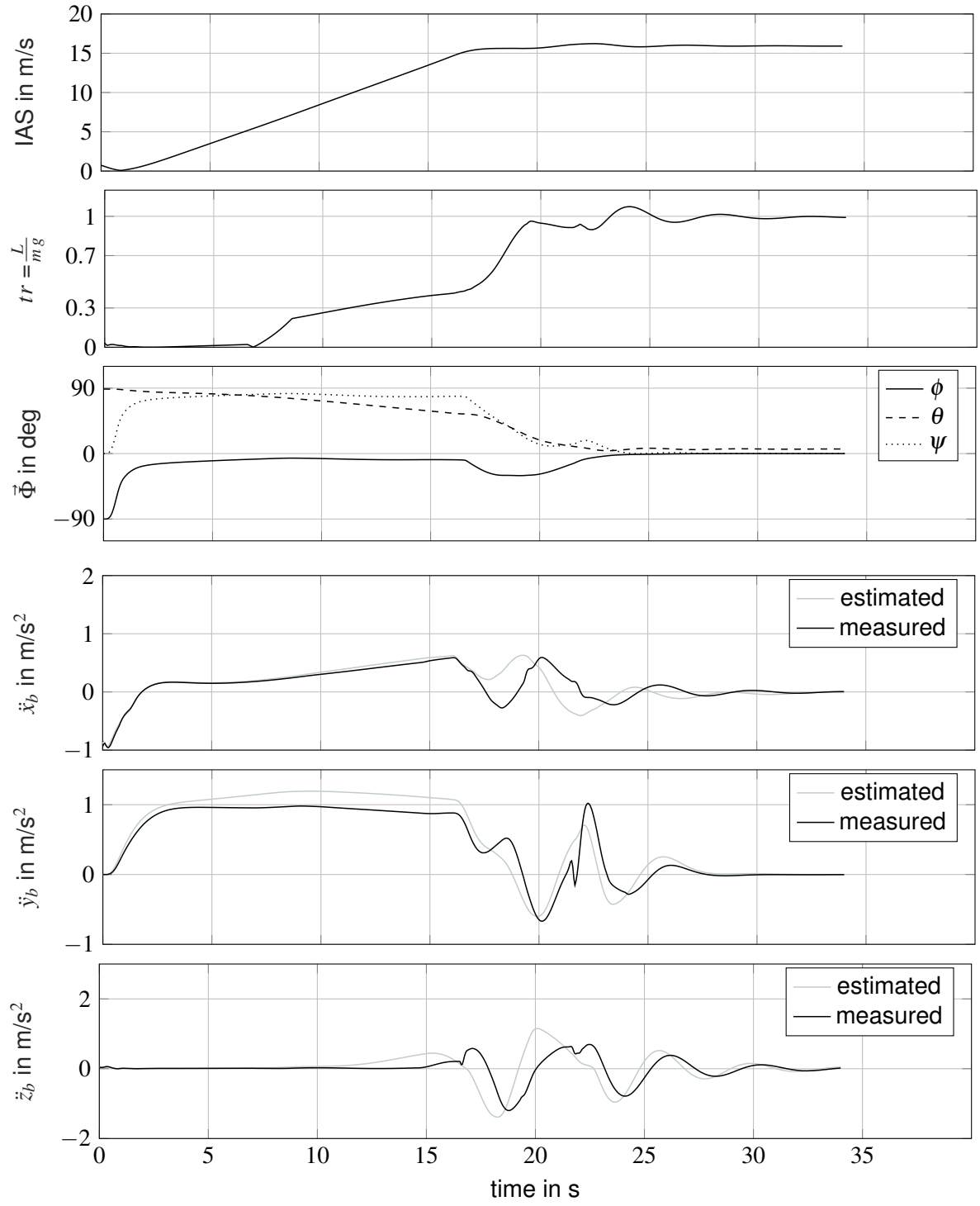

Figure 10 – Simulation results for the dynamic straight yaw-roll transition from prop- to wing-borne flight. tr takes into account the transition ratio, which is the fraction of lift to gravitational load. For a prop-borne flight, tr is close to 0, while for a wing-borne flight it is approximately 1.

The second scenario depicted in Fig. 11a is a tethered curved flight in a wind field. After a vertical takeoff, the flying wing hovers to the transition height, which is 30 m above the VTOL zone. It then accelerates upwind to an airflow of 16 m/s while performing a curved yaw-roll transition. Afterward, the tether is stretched, and a control of the tether force is activated. This is possible because the implemented translational INDI controller allows an acceleration command as an input. To focus on the performance of the translational controller for this second scenario, a constant wind speed of 4 m/s with no gusts is assumed. Figure 11b shows a visualization of this simulation.

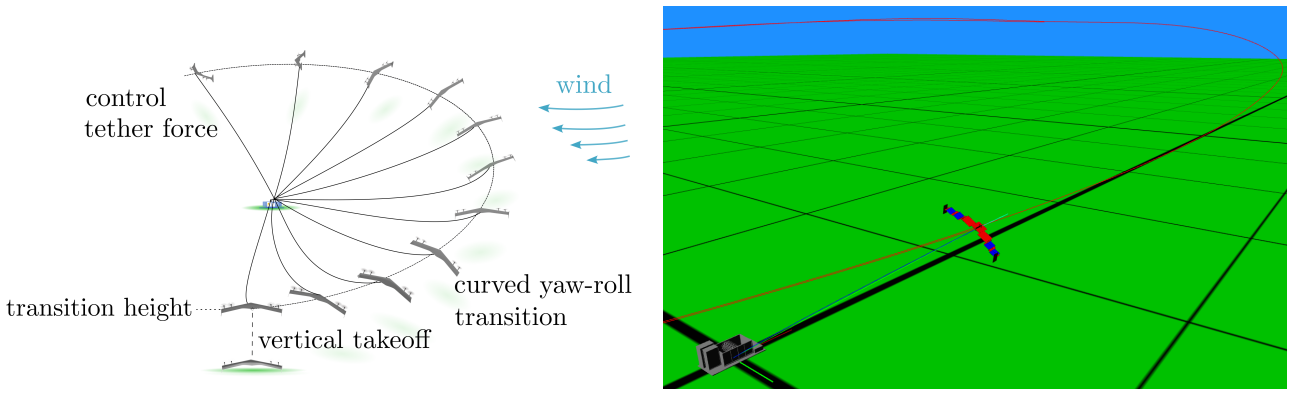

(a) Guidance path

(b) Visualization of the simulation

Figure 11 – Circular guidance path for dynamic transition from prop- to wing-borne flight followed by a tether control phase. The entire flight is performed under the influence of a constant wind field.

As shown in Fig. 12, the yaw-roll transition can also be performed on a curved path in a wind field. Again, a wing-borne flight can be achieved. In contrast to the straight yaw-roll transition, the transition ratio reaches values greater than 1 because the lift must compensate for the tether load and increased gravitational loads from a curved flight. During this transition, the magnitude of the accelerations is about four times greater than for the straight yaw-roll transition.

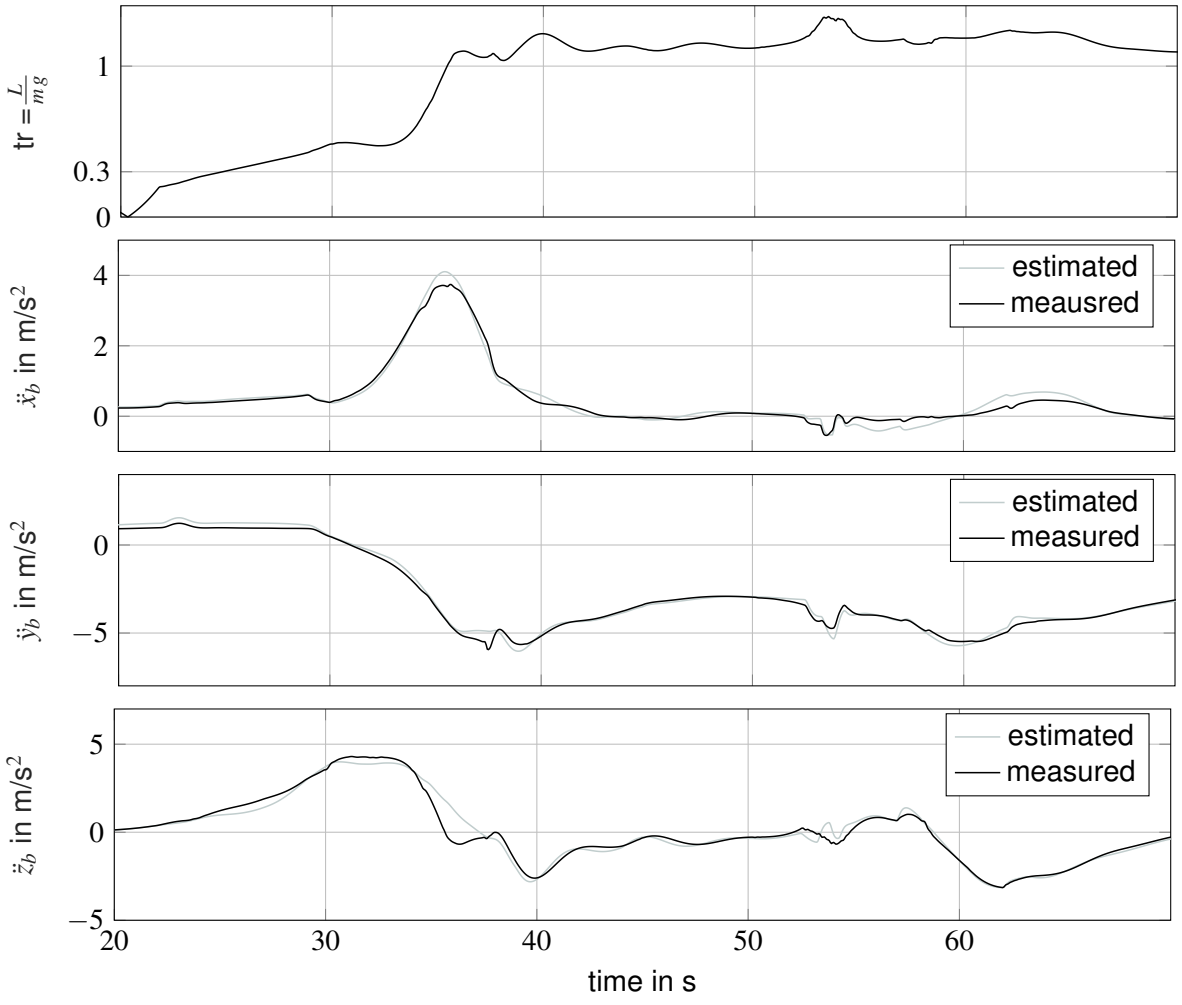

Figure 12 – Simulation results for curved yaw-roll transition

In addition, for this curved flight, the estimated and measured y_b-accelerations decrease to a constant offset. This offset correlates to the centrifugal acceleration for the curved flight under consideration. Again, there is a strong correlation between the estimated and the measured acceleration. For the transition time frame of (20 s - 40 s), the integrated squared error is 0.33 m^2/s^3 and 1.60 m^2/s^3 for x_b- and y_b-direction and 5.92 m^2/s^3 for z_b-direction. As for the straight transition, the error in z_b-direction is the most significant. Nevertheless, a clear correlation between estimated and measured acceleration can be identified for the presented maneuver.

Figure 13 shows the simulation results for a later time frame, where the tether is stretched, and the flying wing is in an aerodynamic wing-borne flight. Again, the centrifugal load can be recognized in the constant offset in the acceleration in y_b-direction. A slow oscillation can also be identified since the observed time frame is larger. This oscillation corresponds to the circulation around the winch. The ground speed is reduced whenever the flying wing is upwind, resulting in lower centrifugal loads. However, the flying wing must accelerate in downwind conditions to maintain an airspeed of 16 m/s. Thus, the ground speed and the centrifugal acceleration increase, resulting in a slow oscillation.

Unlike the previous results, Fig. 13 plots the measured and commanded tether force. As can be seen, the tether force can be controlled with deviations of less than 5 N for the given scenario. It can also be seen that the transient oscillation of the measured tether force is slightly reduced for higher commanded tether loads. The tether force commands can also be identified as small spikes in the estimated acceleration (filtered commanded acceleration) in the y_b- and z_b-directions. For a represen-

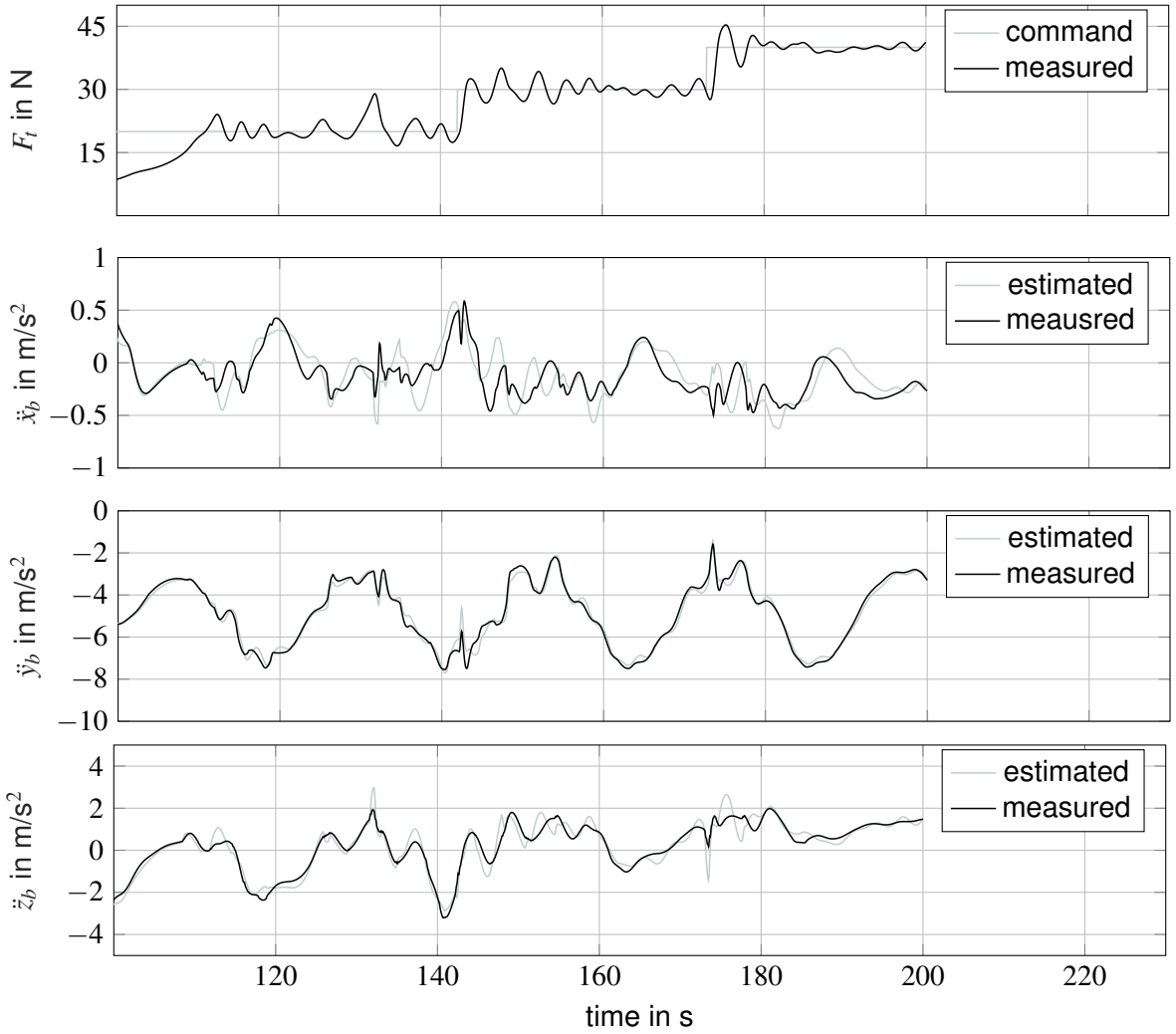

Figure 13 – Simulation results for wing borne flight with active tether force control

tative time frame from 140 s to 160 s, considering a command step from 20 N to 30 N, the integrated square error in x_b- and y_b-direction is 0.89 m^2/s^3 and 2.23 m^2/s^3, while the one in z_b-direction is again the most significant with 4.10 m^2/s^3. This means that the order of this quadratic quality criterion is comparable to that of the curved transition for the same time frame length. In addition, the estimated and measured accelerations in all three axes show a strong correlation. Thus, this second scenario also shows that the assumption of neglecting the tether load in the control effectiveness is appropriate for wing-borne tethered flight and further proves the validity of the translational INDI control concept.

3.5 Analysis of INDI controller via flight tests

The first flight test was recently performed with this controller (see Fig. 7). Only position and velocity were commanded during this test, while the flying wing remained in a prop-borne hover flight. Again, the estimated and measured translational accelerations are observed to analyze the performance of the translational controller. As shown in Fig. 14, the errors are small, and the estimated and measured signals correlate throughout the flight. Different position and velocity steps were commanded during the test, leading to spikes in the acceleration signals. For example, a position respectively velocity command in the wing fixed y_b-direction leads to a peak in the y_b-acceleration. The velocity commands during the flight test were below 3 m/s, and the flight was not exposed to high wind disturbances (measured wind speed below 2 m/s). Therefore, these maneuvers can be considered less highly dynamic than those shown in the simulations. However, when considering the control quality criterion for estimated and measured acceleration, the control performance of the flight test is comparable to that of the simulations. For a time frame from 80 s to 100 s, the integrated quadratic error is 0.21m^2/s^3 in x_b-direction, 1.06m^2/s^3 in y_b-direction, and 1.46m^2/s^3 in z_b-direction. This shows that the control quality criteria for all three axes are in the same order as those from the simulations. As for the simulations, it also shows that the control performance in the x_b-axis is better than in the other two axes. Despite the control deviations observed, this flight proves that the control concept

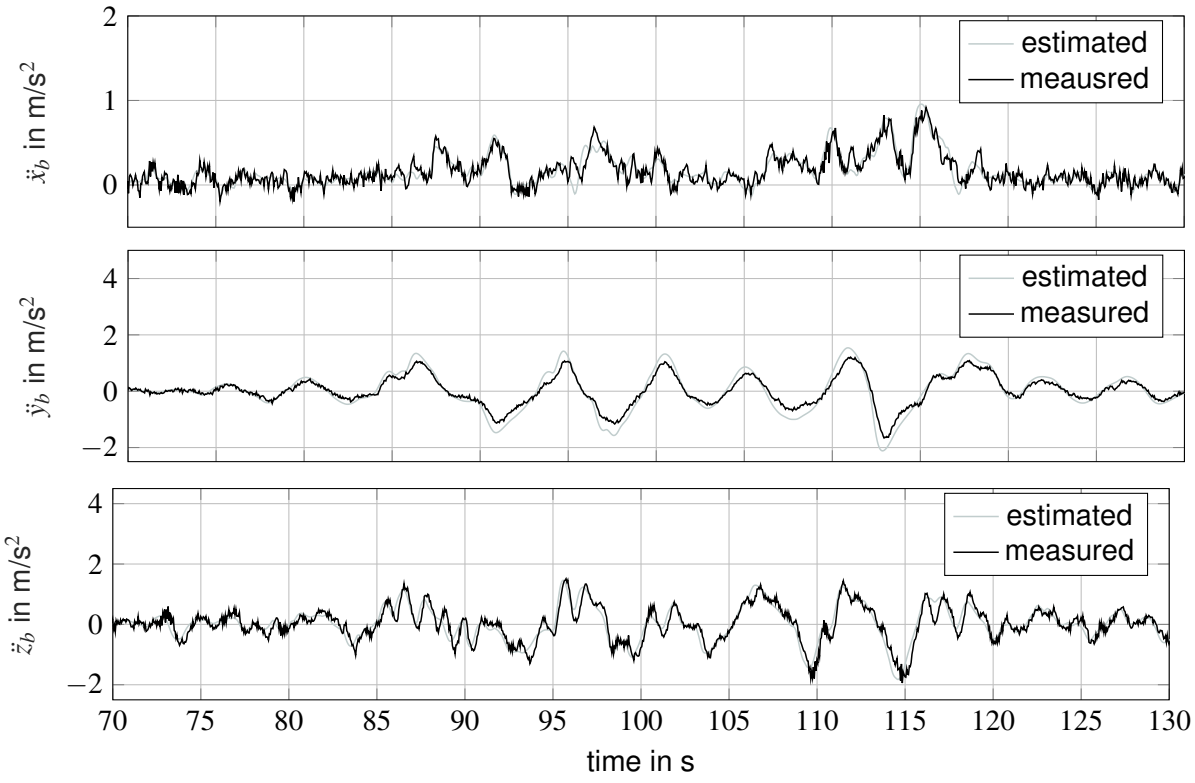

Figure 14 – Estimated and measured translational accelerations in body frame from the first flight test with the translational INDI controller active. During the observed flight phase, the guidance controller sets the velocity and position commands.

works for a hover flight. Further tests with higher airspeed and more dynamic maneuvers, such as the aimed yaw-roll transition, must be performed in future work.

4. Conclusion and Outlook

This research aims to illustrate the design of a translational motion controller applied to a flying wing embedded in an airborne wind energy system. Given the unique challenges of this operational context, this study introduces an incremental nonlinear dynamic inversion based controller with an incremental formulation of control effectiveness. A notable feature of this approach is its universal applicability, which enables unconventional dynamic maneuvers for such specific flight system. It allows the execution of multi-axial maneuvers, including the seamless yaw-roll transition from a propeller-borne hover flight to an aerodynamic wing-borne flight. In addition, this paper investigates the performance and limitations of this approach. The first analysis shows the general correspondence between the control effectiveness used in the controller and that obtained from model linearization. However, it was found that the formulated effectiveness for the thrust was more accurate than the effectiveness for aerodynamics. An explanation for this can be found in the assumptions used to derive the aerodynamic effectiveness, e.g., the assumption of a constant angle of attack along the entire wing instead of a locally variable angle of attack. The derivation of the thrust effectiveness does not require such assumptions, allowing a better match between the effectiveness from controller and that from model linearization. Moreover, results from nonlinear model-in-the-loop simulations with the presented translational control are presented, showing that the measured acceleration correlates well with the estimated acceleration (based on the command). In addition, the results of an initial flight test with this controller are detailed. The control performance is validated and compared using the integrated squared error of the estimated and measured accelerations for the simulation and flight test results. It is shown that the accelerations in the x_b-axis, which are mainly affected by the thrust, show the strongest correlation. Overall, the results prove the functionality of the control concept.

Future work will focus on aspects revealed by the analysis. Some of these involve improving the controller design, while others involve further validating tests:

- This work already considers the damping effect. However, a more detailed study of the damping effect for different flight states and a more sophisticated design of the tailored damping compensation that also considers coupled damping effects can be approached.
- Assumptions are made in the formulation of the aerodynamic effectiveness. An extended formulation of the aerodynamic effectiveness can be developed to include local variations in the angle of attack due to propeller wake flow. Although such an extension of the effectiveness matrix is likely to be complex, it can further improve the quality of the controller.
- Future research can evaluate the stability limits for the different weighting parameters using a linearization of the controlled system with control allocation. In this work, the weighting parameters are fixed values. Future work can identify appropriate weighting parameters that will allow faster attainment of the desired command while maintaining translational control performance. In this context, an overall stability analysis of the flight controller can be performed. Such a linear analysis can also analyze the system's robustness to model uncertainties.
- Flight tests at higher airspeed are required to validate the translational control approach further. The airflow measurement unit must be progressively validated as part of these tests.
- Based on this work, optimized trajectories for launching, energy-harvesting flight and landing with strong winds can be used to validate the presented translational control concept further.

5. Contact Author Email Address

D. F. Duda is responsible for the controller development, overall implementation and documentation. H. Fuest, J. Müller, T. Islam, and D. Moormann contributed to the conceptual design of the controller. For questions about the paper's content, please contact D. F. Duda: duda@fsd.rwth-aachen.de

6. Copyright Statement

References

[1] Uwe Ahrens, Moritz Diehl, and Roland Schmehl. *Airborne Wind Energy -Book*. 2013.

[2] Antonello Cherubini, Andrea Papini, Rocco Vertechy, and Marco Fontana. Airborne Wind Energy Systems: A review of the technologies. *Renewable and Sustainable Energy Reviews*, 51:1461–1476, 2015.

[3] Miles L. Loyd. Crosswind Kite Power. *Journal of energy*, 4(3):106–111, 1980.

[4] R. Martinez-Val. Flying Wings. A New Paradigm for Civil Aviation? *Acta Polytechnica*, 47(1), 2007.

[5] Karl Wohlfahrt and Michael Nickel. *Schwanzlose flugzeuge : ihre auslegung und ihre eigenschaften*, volume 3. Springer-Verlag, 1990.

[6] Jianjian Liang, Qing Fei, Bo Wang, and Qingbo Geng. Tailsitter VTOL flying wing aircraft attitude control. *Proceedings - 2016 31st Youth Academic Annual Conference of Chinese Association of Automation, YAC 2016*, pages 439–443, 2017.

[7] Robin Ritz and Raffaello D'Andrea. A global controller for flying wing tailsitter vehicles. *Proceedings - IEEE International Conference on Robotics and Automation*, pages 2731–2738, 2017.

[8] H. Fuest, D. F. Duda, T. Islam, and D. Moormann. Flight path and flight dynamic analysis of the starting procedure of a flying wing as airborne wind energy system. *Deutscher Luft- und Raumfahrtkongress, Braunschweig Germany 2023*, 2023.

[9] J. Müller, D. Schatten, D. F. Duda, and D. Moormann. Cascaded Indoor Flight Controller Design for a Miniaturized Tiltwing Aircraft. *IMAV 2023: International Micro Air Vehicle Conference and Competition 2023, Aachen, Germany, September 11-15, 2023*, 2023.

[10] Fabian Binz. *Robust, Fault-Tolerant Control of Aircraft with Hovering Capability*. PhD thesis, RWTH Aachen Univeristy, 2020.

[11] Barton J. Bacon and Aaron J. Ostroff. Reconfigurable flight control using nonlinear dynamic inversion with a special accelerometer implementation. *AIAA Guidance, Navigation, and Control Conference and Exhibit*, (August), 2000.

[12] Aaron J. Ostroff and Barton J. Bacon. Enhanced NDI strategies for reconfigurable flight control. *Proceedings of the American Control Conference*, 5:3631–3636, 2002.

[13] E. J.J. Smeur, G. C.H.E. de Croon, and Q. Chu. Cascaded incremental nonlinear dynamic inversion for MAV disturbance rejection. *Control Engineering Practice*, 73(January):79–90, 2018.

[14] Ola Härkegård. Efficient active set algorithms for solving constrained least squares problems in aircraft control allocation. *Proceedings of the IEEE Conference on Decision and Control*, 2(December):1295–1300, 2002.

[15] Ewoud J.J. Smeur, Qiping Chu, and Guido C.H.E. De Croon. Adaptive incremental nonlinear dynamic inversion for attitude control of micro air vehicles. *Journal of Guidance, Control, and Dynamics*, 39(3):450–461, 2016.

[16] H. Fuest, D. F. Duda, T. Islam, T. Ostermann, and D. Moormann. Stabilization of the vertical take-off of a rigid flying wing for an airborne wind energy system. *CEAS Aeronautical Journal*, 12(4):895–906, 2021.

[17] Ken Shoemake. Animating rotation with quaternion curves. 19(3):245–254, 1985.

[18] Boyang Li, Weifeng Zhou, Jingxuan Sun, Chih Yung Wen, and Chih Keng Chen. Development of model predictive controller for a tail-sitter VTOL UAV in hover flight. *Sensors (Switzerland)*, 18(9):1–21, 2018.

[19] Ezra Tal, Gilhyun Ryou, and Sertac Karaman. Aerobatic Trajectory Generation for a VTOL Fixed-Wing Aircraft Using Differential Flatness. *IEEE Transactions on Robotics*, 39(6):4805–4819, 2023.

[20] Ewoud J.J. Smeur, Murat Bronz, and Guido C.H.E. de Croon. Incremental control and guidance of hybrid aircraft applied to a tailsitter unmanned air vehicle. *Journal of Guidance, Control, and Dynamics*, 43(2):274–287, 2020.

[21] Jan Wendel. *Integrierte navigationssysteme: sensordatenfusion, GPS und inertiale navigation*. Oldenbourg Wissenschaftsverlag GmbH, 2007.

[22] Philipp Hartmann. Vorausschauende Flugbahnregelung für Kippflügelflugzeuge Predictive Flight Path Control for Tilt-Wing Aircraft. 2017.

[23] Massimo Pizzol. Github repository "Carbon-Footprint-intermodal", 2019.